

Pruning Sparse Tensor Neural Networks Enables Deep Learning for 3D Ultrasound Localization Microscopy

Brice Rauby, *Graduate Student Member, IEEE*, Paul Xing, *Graduate Student Member, IEEE*, Jonathan Porée, *Member, IEEE*, Maxime Gasse, Jean Provost, *Member, IEEE* (Corresponding author: JeanProvost.)

Abstract—Ultrasound Localization Microscopy (ULM) is a non-invasive technique that allows for the imaging of microvessels *in vivo*, at depth and with a resolution on the order of ten microns. ULM is based on the sub-resolution localization of individual microbubbles injected in the bloodstream. Mapping the whole angioarchitecture requires the accumulation of microbubbles trajectories from thousands of frames, typically acquired over a few minutes. ULM acquisition times can be reduced by increasing the microbubble concentration, but requires more advanced algorithms to detect them individually. Several deep learning approaches have been proposed for this task, but they remain limited to 2D imaging, in part due to the associated large memory requirements. Herein, we propose to use sparse tensor neural networks to reduce memory usage in 2D and to improve the scaling of the memory requirement for the extension of deep learning architecture to 3D. We study several approaches to efficiently convert ultrasound data into a sparse format and study the impact of the associated loss of information. When applied in 2D, the sparse formulation reduces the memory requirements by a factor 2 at the cost of a small reduction of performance when compared against dense networks. In 3D, the proposed approach reduces memory requirements by two order of magnitude while largely outperforming conventional ULM in high concentration settings. We show that Sparse Tensor Neural Networks in 3D ULM allow for the same benefits as dense deep learning based method in 2D ULM i.e. the use of higher concentration *in silico*

and reduced acquisition time.

Index Terms—Deep Learning, 3D imaging, Ultrasound Localization Microscopy (ULM), Sparse Tensor Neural Networks

I. INTRODUCTION

Ultrasound Localization Microscopy (ULM) is an imaging method that non-invasively maps the vascular tree and blood velocities at depth *in vivo*. By localizing and tracking individual microbubbles injected into the blood flow [1, 2], ULM achieves an imaging resolution approximately equal to one tenth of the diffraction-limited resolution. More recently, Dynamic Ultrasound Localization Microscopy (DULM) [3, 4] has extended the capabilities of ULM by enabling the generation of retrospectively-gated, super-resolved movies of the blood flow dynamics, with applications in pulsatility mapping [3], functional imaging of the brain [5], and cardiac imaging [4]. ULM and DULM have been extended to 3D imaging [6, 7, 8, 9] using fully addressed or multiplexed array probes. Both localization and velocity estimation can be improved by rejecting microbubbles that do not appear across several frames [1]. Such tracking can be performed, e.g., using the Nearest Neighbor algorithm [3, 1] or the Hungarian method [10, 11]. Some approaches have also incorporated Kalman filtering to refine the position estimations of a track [6, 9, 12, 13]. The acquisition time necessary to construct a complete vascular map is mainly dependent on the required time to perfuse all vessels and, thus, on microbubble concentration [14]. However, a trade-off exists between the microbubble concentration and the localization precision and accuracy [15], which can be partially lifted using, e.g., methods based on the compressed sensing theory [16], on the division of the k-space in several subregions [17], or tracking the microbubble signals prior to sub-pixel localization [18]. Deep learning-based methods have also investigated frame-by-frame, spatial-only approaches [19, 20, 21], and, more recently, the spatio-temporal context through convolution [22, 23] or sequential modeling [24].

Despite promising results with increased microbubble concentrations both *in silico* [22] and *in vivo* [22, 23], deep-learning based approaches have been limited to 2D imaging. Indeed, the addition of a third spatial dimension considerably increases the size of intermediate feature maps and highly-resolved outputs. For example, a straightforward implementation of Deep-stULM [22] in 3D would require at least two

This work was supported in part by the Institute for Data Valorization (IVADO), in part by the Canada Foundation for Innovation under Grant 38095, in part by the Canadian Institutes of Health Research (CIHR) under Grant 452530, and in part by a Natural Sciences and Engineering Research Council of Canada (NSERC) discovery grant (RGPIN-2020-06786). The work of Brice Rauby was supported in part by IVADO, and in part by the TransMedTech Institute, and in part by the Fonds de recherche du Québec—Nature et technologies. The work of Paul Xing was supported by IVADO and in part by the TransMedTech Institute. The work of Jonathan Porée was supported in part by IVADO, in part by the TransMedTech Institute, and in part by the Canada First Research Excellence Fund (Apogée/CFREF). This research was enabled in part by support provided by Calcul Québec (calculquebec.ca) and the Digital Research Alliance of Canada (alliancecan.ca)

B. Rauby is the Department of Engineering Physics, Polytechnique Montréal, Montréal, QC H3T 1J4, Canada, and also with Mila-Quebec artificial intelligence institute, Montréal, QC H2S 3H1, Canada (email: brice.rauby@polymtl.ca)

P. Xing, and J. Porée are with the Department of Engineering Physics, Polytechnique Montréal, Montréal, QC H3T 1J4, Canada (e-mail: first-name.lastname@polymtl.ca)

M. Gasse is with ServiceNow, Montréal, QC H2S 3G9, Canada, also with the Department of Computer Engineering and Software Engineering, Polytechnique Montréal, Montréal, QC H3T 1J4, Canada, and also with Mila-Quebec artificial intelligence institute, Montréal, QC H2S 3H1, Canada (e-mail: maxime.gasse@servicenow.com)

J. Provost is with the Department of Engineering Physics, Polytechnique Montréal, Montréal, QC H3T 1J4, Canada, and also with the Montreal Heart Institute, Montréal, QC H1T 1C8, Canada (email: jean.provost@polymtl.ca)

Manuscript received XXXX XX, 202X; revised XXXX XX, 202X.

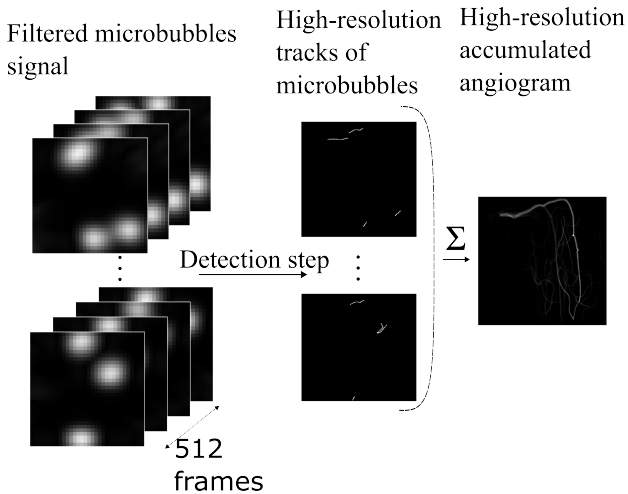


Fig. 1. The left column represents the filtered microbubble signal (i.e., the input of the network), the center column represents the corresponding microbubble tracks (i.e., the desired output of the network) and the right column represent the final result after summation of all the predictions from a dataset (i.e., the vascular structure imaged)

orders of magnitude more memory than its 2D counterpart. Thus, the development of deep learning based models for 3D ULM is conditioned on successfully addressing their memory complexity.

To improve the scaling of memory complexity of deep learning approaches in ULM, we propose to leverage the recently introduced Sparse Tensor Neural Networks [25]. Indeed, while ultrasound images are typically dense data that cannot be stored directly as sparse tensors efficiently, filtered microbubbles responses are sparsely distributed in space and time. One must thus design a filter that extracts microbubble responses from ultrasound images and is sufficiently restrictive that it enhances memory requirements without discarding information enables the neural network to outperform conventional approaches. Hereafter, filtering out most of the input signal from dense tensors before conversion to sparse format while keeping the signal of interest is designated as the dense-to-sparse operation (represented in dashed green in Figure 2).

Our contributions can be summarized as follows:

- A sparse formulation of Deep-stULM outperforming conventional ULM in 2D.
- A comparative study *in silico* between ULM and the proposed approach under varying concentrations in 3D.
- A 2-D *in silico* study of performance and memory usage of dense-to-sparse conversion strategies.

We show that Sparse Tensor Neural Networks reduce memory cost and scale better with added input dimensions, which allows for the training of 3D ULM models with a limited impact on the performance when compared to dense architectures. We also provide the code and the dataset needed to reproduce the results at <https://github.com/provostultrasoundlab/SparseTensorULM>.

II. THEORY

After image formation, ULM data is typically filtered to remove the signal from the tissue while retaining microbubble

responses. In this study, we focus on the subsequent step, which is to find the sub-resolution positions of the microbubbles based on their response. Several deep learning approaches [19, 20] use convolutional architectures where the microbubble position is projected onto a grid with a finer resolution than the input signal. The upscaling factor r between the input dimension and the output dimension typically ranges from 4 to 8. Therefore, the memory complexity for storing the output grid of such architectures in dense format scales with :

$$(r \times D)^d$$

where d is equal to 2 (resp. 3) for 2D (resp. 3D) imaging and D is a typical dimension of the input in pixels. However, ULM is based on the assumption of a sparse distribution of microbubbles. An upper bound on the number of microbubbles that can be detected in a certain volume is given by :

$$N < \left(\frac{\rho D}{\alpha}\right)^d$$

where N is the number of microbubbles, ρ is the size of a pixel in wavelength, and α approximately describes the size of the point spread function in wavelengths. In sparse format, the memory complexity of storing the microbubble positions scales with $d \times N$ and thus it is upper-bounded by:

$$d \times \left(\frac{\rho D}{\alpha}\right)^d$$

Consequently, the ratio between the sparse and the dense representation of the outputs of the networks scales with :

$$d \left(\frac{\rho}{\alpha r}\right)^d \quad (1)$$

For example, with typical values $\alpha = 3$ and $\rho = \frac{1}{2}$, the ratio between the sparse and the dense representation of an ideal outputs from such network is expected to be multiplied by $\frac{3}{2} \frac{\rho}{\alpha r} \simeq \frac{1}{32} = 3.1 \times 10^{-2}$ when extending from 2D to 3D. This scaling law makes the sparse representation very attractive for the extension in 3D.

However, practical factors such as the variability of the upscaling factor r within the network architecture, the reduced sparsity of intermediate representations, the non-uniform distribution of microbubbles in space, or temporal context considerations, can alter this scaling law.

III. METHOD

First, we detail the approach used to simulate the 2D and 3D datasets used for training evaluation of the different method. Then we describe the model architecture, training parameters and evaluation metrics. Additional studies on the impact of the dense-to-sparse operations and on further architecture modifications such as pruning [26] (represented in gold dotted line and scissors in Figure 2) and deep-supervision [27] are presented.

A. Simulations

1) *2D dataset*: To compare Sparse Tensor Neural Networks with their dense counterpart, we based our study on a previously introduced dense method [22] and used the

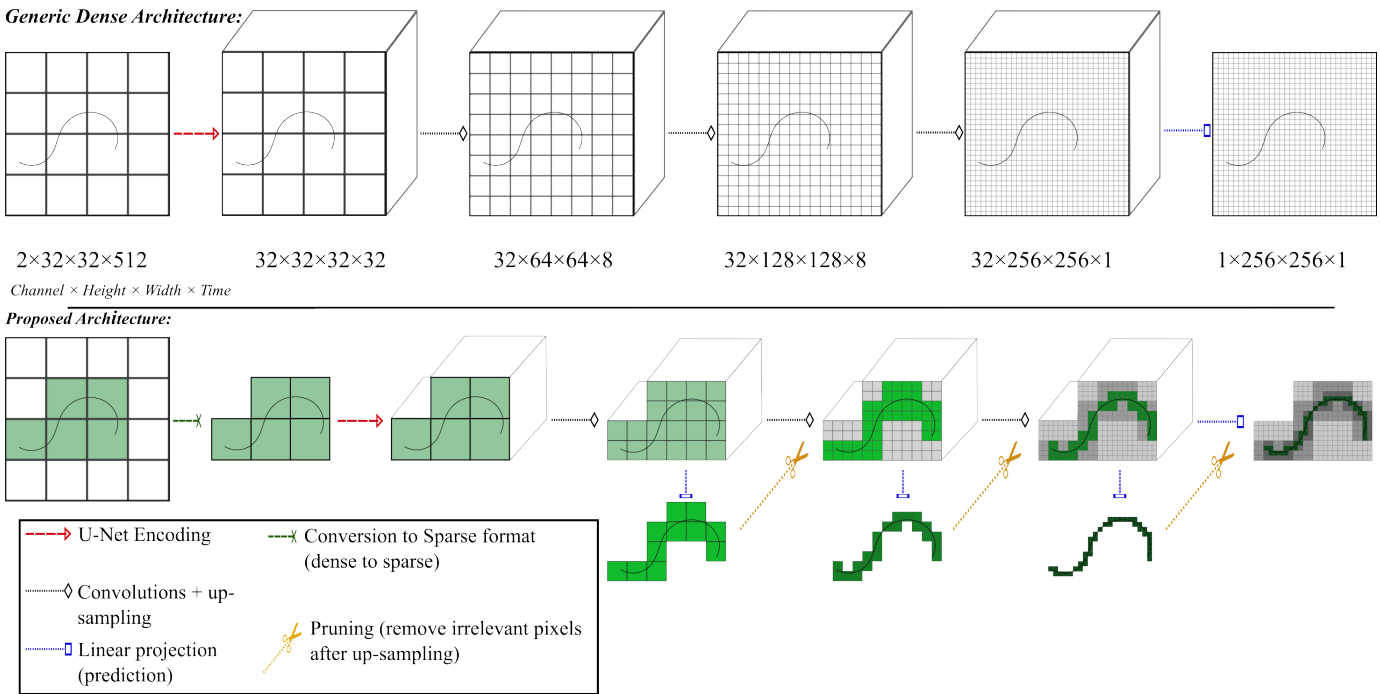


Fig. 2. The top row shows a dense representation of a trajectory in Deep-stULM as well as the intermediate map dimension. The bottom row illustrates how sparse formulations could reduce the memory cost: the green pixels represent the pixels of interest at each resolution, and the gray pixels represent the pixels removed through pruning based on intermediate prediction

same 2D dataset based on the previously published simulation pipeline. Microbubble flow was simulated using a realistic model [15] based on *ex vivo* mice brains obtained with two-photon imaging. Four portions of different mice brains were used to generate the training set, one other portion was used for model selection and validation and the last one was kept as a test set to assess the performance. Since each region covers a volume of only $500 \times 500 \times 500 \mu\text{m}^3$, we diluted the vascular network by a factor of 2 to fill a $1000 \times 1000 \times 1000 \mu\text{m}^3$ area, as done previously [22]. The ultrasound signal corresponding to the microbubble position was simulated using an in-house GPU implementation of SIMUS [28] with parameters corresponding to an L22-14 probe (Vermon, Tours). Three 15.625-MHz, tilted plane waves with angles of -1° , 0° , and 1° were simulated with a frame rate of 1 kHz. The simulated signal was subsampled to match the 100% bandwidth IQ signal, mimicking the Verasonics Vantage system. Finally, the IQ data were beamformed with a GPU implementation of the delay and sum algorithm on a grid of 32×32 pixels with a resolution of $\frac{\lambda}{4}$ (i.e., $25 \mu\text{m}$), in groups of 512 frames. The point spread function (PSF) of the system was simulated at the center of the grid and used to compute the local correlation between the beamformed IQ data with the PSF. The obtained correlation maps were used as the input for the different deep-learning models. In total, 2250 movies were generated for training, 250 for validation, and 500 for testing. The concentration of microbubbles simulated for the training and validation sets was set to 5 microbubbles per field of view (FOV), as done previously [22]. Several test sets were simulated based on the trajectories from the test angiogram with varying concentrations (1, 5, 10, and 20 microbubbles

per FOV) also matching the test set from the previous study [22].

2) *3D Dataset*: The 3D dataset was obtained similarly but since they contain more parameters, additional microbubble trajectories were included to reduce overfitting. We divided the generated spatio-temporal samples in three groups: 3500 samples for training, 500 for the validation, and 2000 for testing. We diluted the vascular network by a factor of 8 to account for the larger wavelength and the coarser beamforming grid ($\frac{\lambda}{2}$). We simulated a 750-fps imaging sequence containing 5 angles ($\{-2^\circ, 0^\circ\}$, $\{2^\circ, 0^\circ\}$, $\{-1^\circ, 0^\circ\}$, $\{1^\circ, 0^\circ\}$, $\{0^\circ, 0^\circ\}$) emitted with a 7.8125-MHz center frequency using a matrix array with parameters matching a commercially available 8-MHz 2D matrix probe (Verasonics, WA, USA). The concentration of microbubbles simulated for the training, validation, and test sets was increased to 30 microbubbles (compared to 5 for the 2D-case) per field of view (FOV) given the additional dimension.

B. Model training and evaluation

1) Sparse Tensor Neural Network and 4D convolutions:

After the *dense-to-sparse* operation, the sparse tensor containing the low-resolution signal was given as input to a Sparse Tensor Neural Network implemented using the Python library MinkowskiEngine [25]. For each intermediate layer, Sparse Tensor Neural Networks only apply their convolution and activation on non-zero values, yielding another sparse tensor. Conventional operations used in CNNs are implemented in MinkowskiEngine, leading to a relatively straightforward translation of the model from dense to sparse format. To assess the benefits of sparse formulation, we converted the dense

Deep-stULM architecture to a sparse formulation without additional change, this approach is designated as *Sparse Deep-stULM* hereafter. However, such dense architecture might not take most of the sparse tensor implementation. Pruning or cascaded learning could further improve the memory efficiency of the sparse formulation. Both of these additional modifications require intermediate supervision and are detailed in the following sections. The resulting models are also extended directly to 3D imaging with 4D convolutions to handle 3D+T tensors. 4D convolutions are directly implemented in the Python library MinkowskiEngine [25].

2) *Training procedure*: For the 2D models based on Deep-stULM, the hyperparameters were set to the same value as in the original study [22]: the optimizer used was Adam [29] and the training was divided into two parts. During the first 150 epochs, the ground truth microbubble trajectories were dilated with a radius of 2 to stabilize the training. The initial learning rate was set to 0.1 and then decayed by a factor of 10 at the epochs 15, 45, 75, and 100. During the last 150, the ground truths were no longer dilated, and the learning rate was set to 0.001 at epoch 150 and then decayed by a factor of 10 at epochs 160, 200 and 250. We did not optimize the hyperparameters for the sparse formulation of Deep-stULM and used the same as the original study. The batch size was set to 8 for all the runs in 2D. For the 3D models, we also used the Adam optimizer with an initial learning set of 0.1. We trained the 3D networks for 20 epochs in total, and the learning rate was decayed by a factor of 10 at epochs 15 and 17. For the first epoch, the batch size was set to 2 to allow every configuration to fit in memory, then for the remaining epochs, the batch size was increased to 4.

3) *Performance comparison with ULM and Deep-stULM*:

a) *Evaluation metric*: To compare our results with the previously established method [22] and conventional ULM, we measure the overlap between the network prediction and ground truth using the dice coefficient :

$$\text{Dice} = \frac{2 \times |\text{GT} \cup \text{Pred}|}{|\text{GT}| + |\text{Pred}|}$$

with GT being the projection of all the trajectories from the ground truth to the super-resolved grid and Pred the prediction of the network. Similarly to the previous study [22], the dice values displayed use a dice computed between the binarized angiograms (i.e., between the logical summation of all the microfilms from the test set).

b) *Conventional ULM*: We also provide the results of a standard, non-deep-learning ULM method, described in [3]. Briefly, Gaussian fitting was used to localize microbubbles and the Hungarian method [30] was used for the tracking step. The number of detections in each frame was set to the optimal value based on the number of microbubbles simulated in the FOV (i.e., for the 5MB/FOV concentration, the number of detection would be set to 5). Note that this setting is ideal and may favor the conventional ULM. Indeed, in real applications, the exact number of microbubbles in the FOV is unknown.

c) *Memory monitoring*: We monitored the memory usage of the training using CometML and took the maximum value reached during the training of each method. As there is some

stochasticity involved both in training and in the measurement of the memory, we used the average across 3 different runs and provided the standard deviations between each run for deep learning approaches. For the 3D dense formulation of Deep-stULM, it was not possible to train the model due to practical memory limitation. Therefore, we provide only an estimate of the memory usage. This estimate was based on scaling the 2D memory usage based on the increase of memory for the intermediate maps due to the addition of a spatial dimension.

C. Additional studies

1) *Dense-to-sparse strategies*: To assess the loss of information and its impact on the performance caused by the dense-to-sparse filtering, we compared the performance of the sparse model for two simple dense-to-sparse strategy referred as Top-k and thresholding strategy with varying value for their respective parameters. To provide better intuition on the performance that one can expect with more sophisticated filtering, we developed a deep learning based solution. To compare between each method, we computed the average number of non-zero pixels in the test set movies to compare across methods and plotted it in Figure 6. In addition, to differentiate between the performance loss induced by the dense-to-sparse strategy from the effect of the sparse implementation, we also evaluated a dense model with inputs filtered according to the dense-to-sparse strategy (each model was retrained on the filtered data).

a) *Top-k strategy*: Typical ULM approaches use regional maxima for microbubble detection before localizing them with high precision [10]. Based on the same underlying assumption that the microbubble signals are located near local maxima, it is reasonable to consider only the k-largest pixel of each input tensor. This operation is designated as top-k operation later on. In practice, due to the smoothness of the input, this approach is very similar to the use of local maxima value while providing better control of the memory usage of the input tensor. The explored values used for the top-k approaches range between 5000 to 50000 pixels.

b) *Thresholding strategy*: Previously published deep-learning methods [22] used a threshold based on the value of the local correlation between the signal and the point spread function of the imaging system to remove residual after clutter filtering *in vivo*. We applied this same approach directly on our simulated datasets. For the thresholding approaches, the threshold values were set to $\{0.01, 0.05, 0.10, 0.25\}$. As the thresholding strategy with a threshold set at 0.10 in 2D offered a good trade-off between performance and sparsity, we used it for all the experiments where the dense-to-sparse strategy was not specified. The threshold was heuristically set to 0.25 for the 3D experiments.

c) *Deep learning based strategy*: We trained a dense CNN to localize microbubbles at low resolution. To do so, it is trained to predict the presence of microbubbles in every pixel of the beamforming grid (low resolution). The dense network used to localize microbubbles at low resolution is fully convolutional both in space and time direction and takes as input a tensor of shape $2 \times H \times W \times T$ in 2D. The inputs channels encode the real and imaginary parts of the input

signal. The input signal is composed of the local correlation of the beamformed IQ data with the simulated PSF of the imaging system. The spatial resolution was kept unchanged throughout the whole network. However, the temporal dimension was reduced by a factor of 2. The output of this network was then interpolated to match the correlation map dimension. The resulting mask is used to convert the correlation map to a sparse format, where only the pixel values with microbubbles are stored along with their coordinates. This filtering network was trained using the dice loss between its predictions and the ideal mask at low resolution obtained from the simulated microbubble position.

2) *Architecture modifications*: Herein, we describe further experiments to refine the sparsity using pruning on the intermediate representation of the network along with deep-supervision and cascaded learning.

a) *Deep Supervision and pruning*: Similarly to other architectures [21, 19, 20], Deep-stULM [22] uses up-sampling layer that preserves the sparsity of the upsampled tensor. This is sub-optimal as at finer resolution the sparsity of the trajectory is increased as depicted in Figure 2. To mitigate these issues, we used the previously introduced pruning operations [26], that aim to gradually remove the pixels where no microbubbles are detected (green pixels versus gray pixels in Figure 2). The feature maps are masked based on the output of an intermediate classifier. Consequently, the removed pixels are no longer considered in the following operation and their coordinates are not stored in memory. As depicted in Figure 2, we implemented pruning at every resolution level based on intermediate prediction. Since pruning requires the training of intermediate classifiers at each level, we trained them in a supervised fashion. These intermediate classifiers are trained using the same loss as the final loss and consist of pointwise convolution directly applied to the intermediate representation of the network. This form of supervision is similar to deep supervision [27] and can also serve as regularization and improve the performance of the network. These intermediate classifiers are required to perform pruning, as they provide the mask used to remove the less relevant pixels from the following operations.

b) *Cascaded learning*: In the case of super-resolution, deep supervision also makes possible a certain form of cascaded learning inspired by [31]. Indeed, the intermediate classifiers can be trained sequentially: during the first phase of the training, only the first classifier is trained to predict the presence of microbubbles on a grid at the input resolution. Then, during the following phase, the intermediate classifiers corresponding to higher resolution levels are sequentially added to the global loss. When applied, the cascaded learning strategy used one epoch for each intermediate level, and the number of epochs for the last resolution level was the same as in standard training.

IV. RESULTS

A. Memory reduction and performance comparison in 2D

The memory usage results and performance at 5 MB/FOV are reported in Table I for Conventional ULM, Deep-stULM,

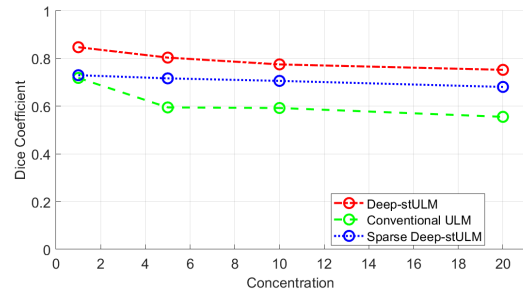


Fig. 3. Evolution of the performance as a function of the concentration

and Sparse Deep-stULM. For the sparse method, the threshold strategy was used to convert the input to sparse formulation. Sparse formulation reduced the memory usage of Deep-stULM from 12.6 GB to 6.8 GB during training, while the dice decreased from 80.4% to 71.7%. In a similar setting, conventional ULM reached 59.5% of dice. The results of the different methods in 2D under varying concentrations are shown in Figure 4 and the evolution of the dice value computed are reported in Figure 3. Qualitatively, the standard ULM performances degraded as the concentration increased with degradation in resolution starting from 5 microbubbles per field of view (MB/FOV). Quantitatively, this diminution of performance was highlighted by a drop in dice coefficient from 71.9% with 1 MB/FOV to 59.5% for 5 MB/FOV. The performance continued to decrease with the concentration until it reached a dice of 55.2% at 20 MB/FOV with only the biggest vessels being visible. In contrast, the dense Deep-stULM approach exhibited a smaller degradation of performance from 84.7% for 1 MB/FOV to 75.2% for 20 MB/FOV. The sparse formulation of Deep-stULM showed robustness to increased concentration and reached performance levels at high concentration (with a dice coefficient of 70.6% (resp. 68.0%) for 10 (resp. 20) MB per FOV that were very close to its performance level at low concentration (73.0% for 1MB per FOV). However, this performance at low concentration (1MB per FOV) were lower than Deep-stULM (84.7%) but were comparable to conventional ULM (71.9%).

B. 3D feasibility study

In Table I, we display the results and the memory usage for Sparse Deep-stULM and conventional ULM as well as estimated memory usage in 3D for Deep-stULM. The values for the dice in 3D were typically lower as there is more possibility for a non-overlapping trajectory than in 2D. It is important to note that just using the sparse formulation allowed us to train the network with less than 11GB of GPU memory while outperforming conventional ULM (50.0% versus 12.3%). For qualitative analysis, the reconstructed angiograms from the test set are displayed in Figure 5 with concentration increasing from 1 MB/FOV to 30 MB/FOV. At high concentration (10 MB/FOV and 30 MB/FOV), the sparse model accurately reconstructed the angiogram when conventional ULM failed to do so. Indeed, the conventional ULM produced many false detections that were not present

TABLE I
COMPARISON OF THE MEMORY USAGE AND PERFORMANCE SPARSE AND DENSE FORMULATION OF DEEPST-ULM. * VALUE ESTIMATED.

	2D (5MB/FOV)		3D (30MB/FOV)	
	Memory requirements (GB)	Dice (%)	Memory requirements (GB)	Dice (%)
Sparse Deep-stULM	6.8 ± 0.2	71.66 ± 2.35	9.9 ± 0.1	49.97 ± 1.79
Deep-stULM	12.6	80.38 ± 0.19	694*	N.A
ULM	N.A	59.48	N.A	12.34

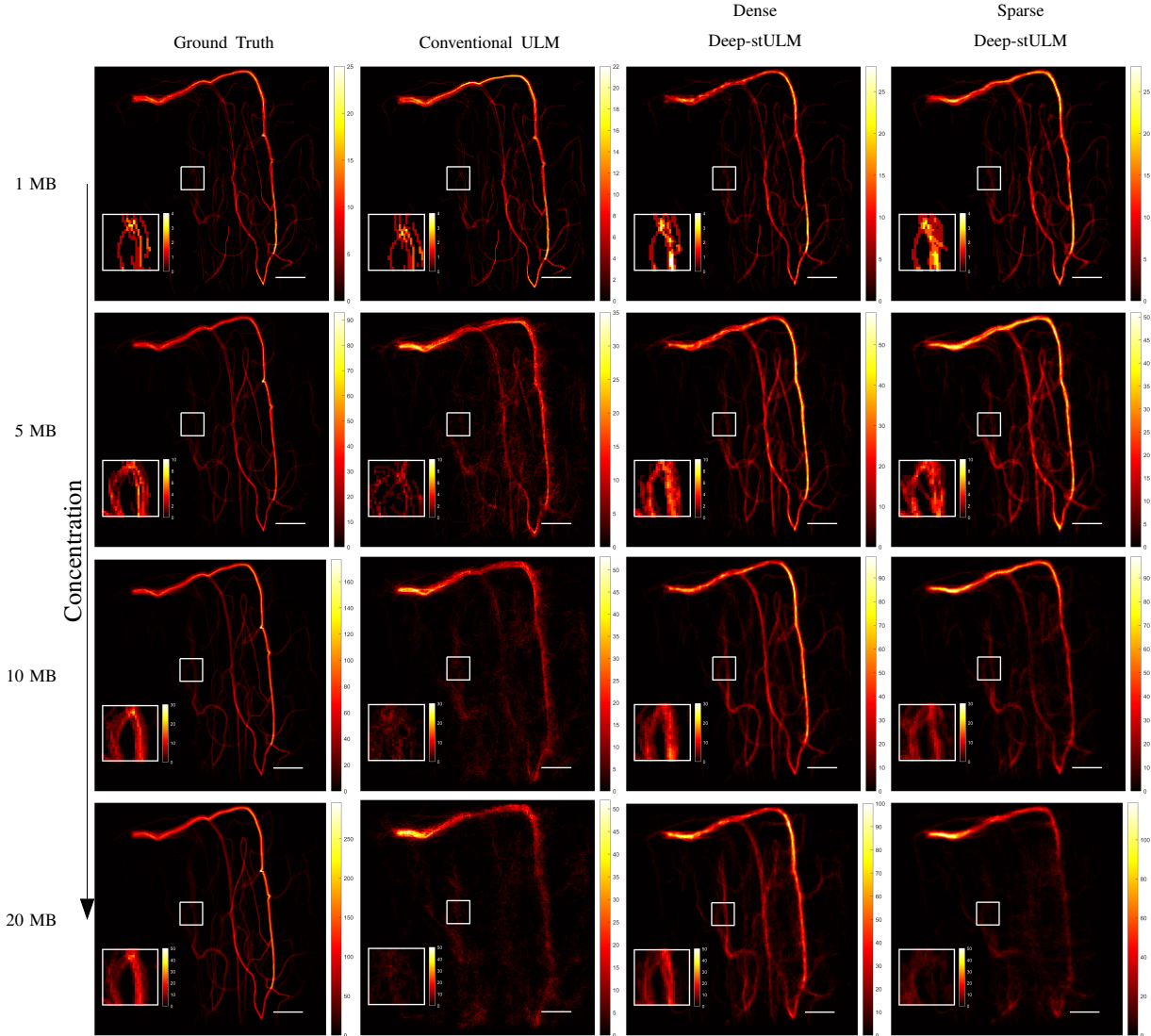


Fig. 4. Comparison of performance under increasing concentration for conventional ULM (center left column), Deep-stULM dense formulation (center right column) and its sparse formulation (right column). Ground truth is given for comparison (left column). Scale bar is 98μ and corresponds to the wavelength of the simulated pulse. Concentration increases from 1 (top row), 5, 10 and 20 (bottom row) microbubbles per field of view.

in the sparse model reconstruction. At low concentration (1 MB/FOV), both conventional ULM and sparse model reconstructed the angiogram with fidelity.

C. Additional studies

1) *Evaluation of strategies to convert to sparse formulation:* In figure 6, it is observed that the thresholding and top-k dense-to-sparse approaches reached a very similar trade-off

between the sparsity obtained and the level of performance independently of the formulation of the model (dense or sparse). Indeed, for the sparse model with the thresholding dense-to-sparse strategy the dice varies from 67.6% with around 21000 pixels to 75.3% with 90000 pixels while it varies from 65.4% with around 5000 pixels to 73.9% with 100000 pixels for the top-k strategy. Similarly, for the dense model with the thresholding dense-to-sparse strategy the dice varies from 79.4% with around 11000 pixels to 79.3% with 90000

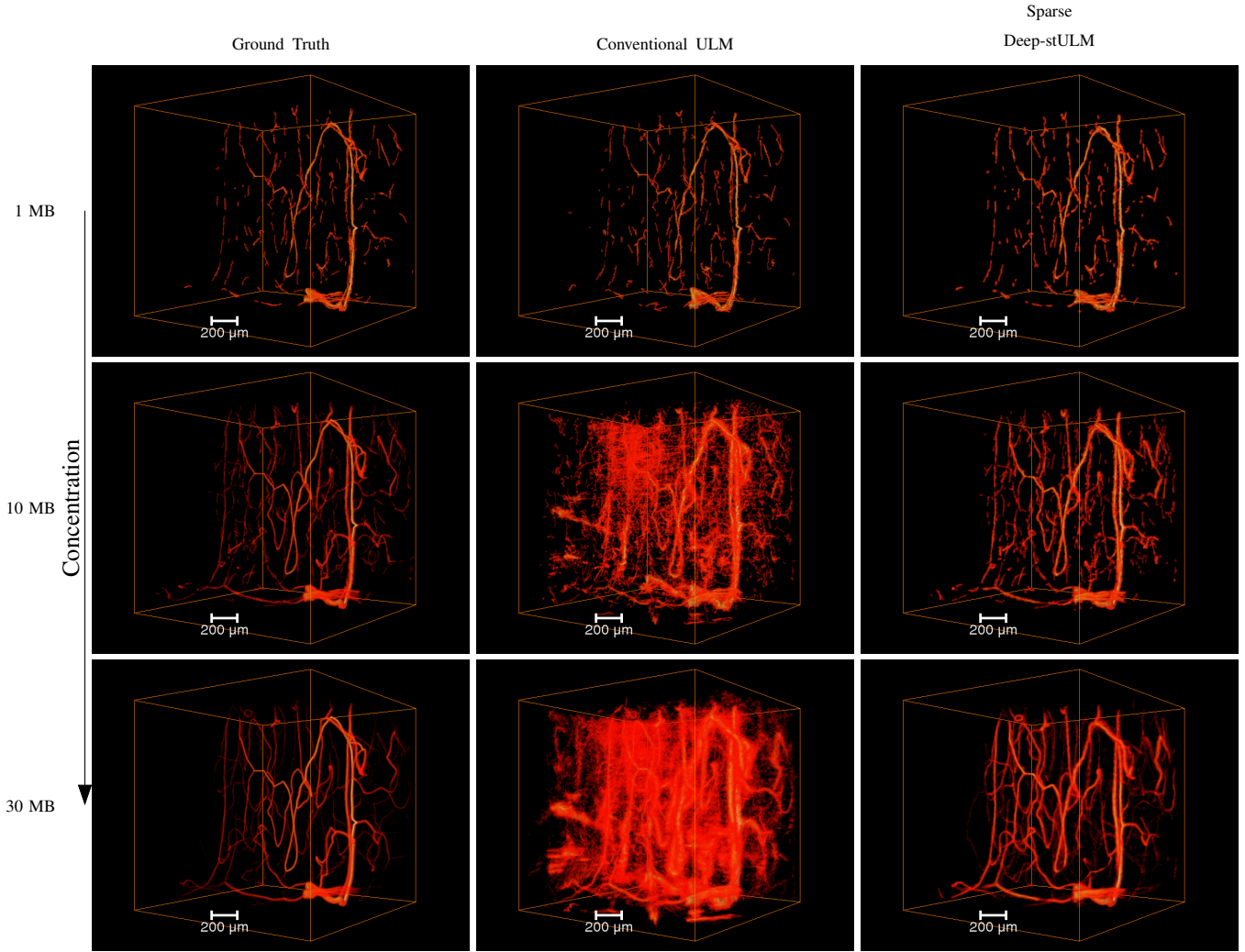


Fig. 5. 3D Comparison of performance under increasing concentration for conventional ULM (center column) and Deep-stULM sparse formulation (right column). Ground truth is given for comparison (left column). Scale bar is $200 \mu\text{m}$ and corresponds to the wavelength of the simulated pulse. Concentration increases from 1 (top row), 10 and 30 (bottom row) microbubbles per field of view.

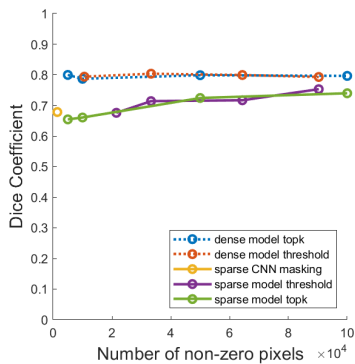


Fig. 6. Evolution of performance as a function of the sparsity achieved for different dense-to-sparse and comparison with dense network with masked input as well as CNN-based dense to sparse operations.

pixels while it varies from 79.9% with around 5000 pixels to 79.6% with 100000 pixels for the top-k strategy. Finally, the CNN dense-to-sparse operation yielded a better trade-off

than all the other approaches. Indeed, the CNN dense-to-sparse operation reached a dice of 67.8% with only 1400 pixels.

2) *Impact of architecture modifications:* In table II, we observed that using pruning jointly with sparse formulation led to a decrease in memory requirements in 2D (6.9 GB to 5.6 GB) but also led to an important degradation of the performance (8.8% of dice). It appeared that combining pruning and cascaded learning has a small impact on the memory (5.6 GB versus 5.7 GB) while degrading the performance (more than 3% of dice). The addition of intermediate loss for deep supervision did not benefit the training performance and had a small memory cost. In 3D, every variation of the model trained significantly outperformed the conventional ULM (between 38% and 50% for the sparse models and 12.3% for the conventional ULM). In contrast to 2D, the use of pruning reduced memory usage by a factor of approximately 4. However, similarly to the 2D case, pruning also degraded the performance (50% to 38.6%).

TABLE II
COMPARISON OF THE MEMORY USAGE AND PERFORMANCE OF THE DIFFERENT ADDITIONS TO SPARSE DEEPST-ULM ARCHITECTURE.

	Sparse input	Intermediate loss	Pruning	Cascaded learning	2D (5MB/FOV)		3D (30MB/FOV)	
					Memory requirements (GB)	Dice (%)	Memory requirements (GB)	Dice (%)
Sparse Deep-stULM + Pruning + cascaded learning	✓	✓	✓	✓	5.6 ± 0.2	58.16 ± 0.77	3.7 ± 0.4	38.53 ± 0.27
Sparse Deep-stULM + Pruning	✓	✓	✓		5.7 ± 0.1	62.85 ± 0.63	3.6 ± 0.2	38.65 ± 0.58
Sparse Deep-stULM + int. loss	✓	✓			6.9 ± 0.1	71.33 ± 0.36	10.6 ± 0.3	43.51 ± 0.99
Sparse Deep-stULM	✓				6.8 ± 0.2	71.66 ± 2.35	9.9 ± 0.1	49.97 ± 1.79

V. DISCUSSION

In this work, we studied the impact of using a sparse formulation on the memory usage and performance of Deep-stULM. We also investigated more multiple methods to further increase sparsity and reduce the memory usage. Our results suggest that solely using the sparse formulation allows for the extension of existing deep learning architectures to 3D ULM, while preserving the performance robustness at high concentration. However, more complex modifications to the architecture had a less important impact on the memory usage while degrading the performance.

A. Reducing memory usage of existing methods in 2D

The sparse formulation offers a relatively simple approach to divide by nearly two-fold the memory requirement of an existing architecture in 2D with little impact on the performance. Indeed, the sparse formulation qualitatively matches the performance on the concentration used during training (5 MB/FOV) and for higher concentration (10 MB/FOV) and quantitatively outperforms conventional ULM by an important margin. Dense formulation of Deep-stULM performs better on very high concentration (20 MB/FOV) and isolated microbubble (1 MB/FOV). As the training set only contains samples at a concentration of 5 MB/FOV, the dense formulation seems to better generalize to unseen data. This better generalization capability and the relatively small size of the training set can also explain the performance gap between the dense and sparse formulation on training concentration, as the dense formulation would be able to better generalize to the test set. Increasing the dataset size and its complexity could bridge the performance gap between the dense and the sparse formulation, while still benefitting from the memory improvements. Top-k and thresholding dense-to-sparse strategies appear to have similar performance. This performance appear to be suboptimal when compared to the performance reached with much fewer pixels by the CNN dense-to-sparse strategy. Presumably, the sparse formulation might benefit from more sophisticated dense-to-sparse strategy to further improve the proposed trade-off between performance and memory requirements in training.

B. Scaling to 3D imaging

In 3D, the sparse formulation allowed for training, with less than 11 GB of memory, an architecture that would require

close to 700GB of memory in dense formulation. As expected, the sparse formulation impact on memory was greater in 3D than 2D. Experimentally, the ratio between the sparse and the dense formulation was multiplied by 2.6×10^{-2} when extending from 2D to 3D whereas the theoretical value from Eq. 1 was 3.1×10^{-2} . The smaller ratio could be explained by the aforementioned experimental factors such as temporal context considerations, as well as the higher threshold for the dense-to-sparse strategy in 3D. The performance gap between the sparse formulation of Deep-stULM and the conventional ULM was larger in 3D, suggesting an even higher potential for deep learning based approach in 3D ULM. On the one hand, the drop of performance of conventional ULM might be caused by the important side lobes of the simulated PSF in 3D. Indeed, these sidelobes create false detection which are supposed to be filtered during the tracking step based on the track length. However, in high concentration, candidate detections in successive frame are multiple causing the filtering on track length to be less effective and contribute to 3D conventional ULM map with a high number of false positives. On the other hand, it is also possible that the additional dimension increases the capability of the deep learning approach to distinguish crossing trajectories, leading to better performance relatively to conventional ULM. The results in 3D shows that akin to the dense approach in 2D, sparse models can accurately reconstruct angiograms at concentration where conventional ULM is failing. When translated in vivo, such performance in high concentration would allow for reduced acquisition time. In 3D, where dataset tends to be larger, reducing acquisition time is even more crucial as it also reduces the storage needed and the associated transfer time.

C. Further reductions of memory and performance trade-off

a) *Dense-to-sparse strategies*: The parameter studies showed that simple strategies for *dense-to-sparse* performed similarly and better trade-off could be achieved with deep-learning based *dense-to-sparse* operations. However, the learned approach for *dense-to-sparse* operation lacked flexibility on the trade-off between sparsity achieved and performance. Increasing the number of pixels considered in the sparse formulation reduced the performance gap between sparse and dense formulation of Deep-stULM. This might suggest sub-optimal dense-to-sparse operations.

b) *Architecture modifications*: It appears that architecture modifications such as deep-supervision, cascaded learning and pruning had an important impact on the performance with smaller gain in memory than that then sole sparse formulation. Cascaded learning and deep-supervision negative impact on the performance could be explained by the fact that microbubble detection at coarse resolution is different from localization at super-resolution and therefore intermediate losses enforce the learning of less relevant latent representations. Considering the additional complexity in training and architecture constraint going with this modifications, it is less clear that they present an interesting trade-off between memory usage and performance.

D. Limitations and perspectives

The proposed method demonstrate sparse tensor neural networks can extend the benefits of deep learning based approach in ULM from 2D to 3D imaging by improving the scaling law of memory costs with dimensionality and resolution. However, some limitations should be mentioned and could be addressed by future studies.

1) *Problem formulation*: This study is mostly focused on measuring the impact of using a sparse formulation in deep learning for ULM. For this reason, it does not tackle some key challenges in framing the learning problem. On the one hand, it is important to mention that even though the dice loss has been proposed and successfully applied in the previous study [22], it is unstable and lacks smoothness when working with temporal projection of trajectories. In addition, the final representation of the prediction, being a projection of the microbubble trajectories on a grid, does not offer the same liberty for downstream analysis as the individual detections provided by conventional ULM. A formulation tackling these issues has been recently proposed [23] based on the DECODE method [32] and could be worth investigating. On the other hand, the encoding of the real and imaginary parts of the input signal as channels lacks the proper arithmetic of complex numbers. Using a complex value neural network [33] could allow a better representation of the signal with less overfitting and better overall performance. Such networks have shown interesting potential when dealing with ultrasound data [34, 35].

2) *Validity of the in silico model*: The proposed approach reaches the level of performance of the state-of-the-art dense model *in silico* under varying concentrations of microbubbles. It would be interesting to evaluate the validity of the conclusions on real data as it has not been tested *in vivo*. However, as the *in vivo* application of both dense and proposed methods requires intensive parameter tuning, it is difficult to ensure a fair comparison between the methods. Additionally, current training datasets for ULM are limited in their diversity and realism. They often require tuned pre-processing, and therefore it is not clear that better learning ability on the simulated dataset would lead to improved performance *in vivo*. Furthermore, as the main benefit of the proposed method is an improvement of the scaling law of the memory complexity, it is reasonable to assume that it is still valid *in vivo*.

VI. CONCLUSION

In this study, we studied the potential of sparse formulation when applying deep learning in 3D ULM. We also proposed further optimization of memory efficiency through pruning of the 3D ULM deep learning model. The proposed Sparse DeepstULM method successfully improve the scaling of memory requirements of deep learning based approaches, addressing the challenge of their extension in 3D. While it comes at a small cost of performance in 2D, the use of deep-learning in 3D ULM seems to be even more beneficial than in 2D. To the best of our knowledge, it is the first application of deep learning for 3D ULM, and it could pave the way for further approaches both *in silico* and *in vivo*. Further applications of such models could allow for improved architectures capable of fitting to more diverse datasets, yielding better results both in 2D and 3D ULM or DynULM.

REFERENCES

- [1] Claudia Errico et al. “Ultrafast Ultrasound Localization Microscopy for Deep Super-Resolution Vascular Imaging”. In: *Nature* 527.7579 (Nov. 2015), pp. 499–502. ISSN: 1476-4687. DOI: 10.1038/nature16066.
- [2] K. Christensen-Jeffries et al. “In Vivo Acoustic Super-Resolution and Super-Resolved Velocity Mapping Using Microbubbles”. In: *IEEE Transactions on Medical Imaging* 34.2 (Feb. 2015), pp. 433–440. ISSN: 1558-254X. DOI: 10.1109/TMI.2014.2359650.
- [3] Chloé Bourquin et al. “In Vivo Pulsatility Measurement of Cerebral Microcirculation in Rodents Using Dynamic Ultrasound Localization Microscopy”. In: *IEEE Transactions on Medical Imaging* 41.4 (Apr. 2022), pp. 782–792. ISSN: 1558-254X. DOI: 10.1109/TMI.2021.3123912.
- [4] Philippe Cormier et al. “Dynamic Myocardial Ultrasound Localization Angiography”. In: *IEEE Transactions on Medical Imaging* (2021), pp. 1–1. ISSN: 1558-254X. DOI: 10.1109/TMI.2021.3086115.
- [5] Noémi Renaudin et al. “Functional Ultrasound Localization Microscopy Reveals Brain-Wide Neurovascular Activity on a Microscopic Scale”. In: *Nature Methods* 19.8 (Aug. 2022), pp. 1004–1012. ISSN: 1548-7105. DOI: 10.1038/s41592-022-01549-5.
- [6] Chloé Bourquin et al. *Quantitative Pulsatility Measurements Using 3D Dynamic Ultrasound Localization Microscopy*. Mar. 2023. DOI: 10.48550/arXiv.2303.14330. arXiv: 2303.14330 [physics].
- [7] Baptiste Heiles et al. “Ultrafast 3D Ultrasound Localization Microscopy Using a 32×32 Matrix Array”. In: *IEEE Transactions on Medical Imaging* 38.9 (Sept. 2019), pp. 2005–2015. ISSN: 1558-254X. DOI: 10.1109/TMI.2018.2890358.
- [8] Arthur Chavignon et al. “3D Transcranial Ultrasound Localization Microscopy in the Rat Brain with a Multiplexed Matrix Probe”. In: *IEEE transactions on biomedical engineering* PP (Dec. 2021). ISSN: 1558-2531. DOI: 10.1109/TBME.2021.3137265.

- [9] U-Wai Lok et al. “Three-Dimensional Ultrasound Localization Microscopy with Bipartite Graph-Based Microbubble Pairing and Kalman-Filtering-Based Tracking on a 256-Channel Verasonics Ultrasound System with a 32×32 Matrix Array”. In: *Journal of Medical and Biological Engineering* 42.6 (Dec. 2022), pp. 767–779. ISSN: 2199-4757. DOI: 10.1007/s40846-022-00755-y.
- [10] Baptiste Heiles et al. “Performance Benchmarking of Microbubble-Localization Algorithms for Ultrasound Localization Microscopy”. In: *Nature Biomedical Engineering* 6.5 (May 2022), pp. 605–616. ISSN: 2157-846X. DOI: 10.1038/s41551-021-00824-8.
- [11] Pengfei Song et al. “On the Effects of Spatial Sampling Quantization in Super-Resolution Ultrasound Microvessel Imaging”. In: *IEEE Transactions on Ultrasonics, Ferroelectrics, and Frequency Control* 65.12 (Dec. 2018), pp. 2264–2276. ISSN: 1525-8955. DOI: 10.1109/TUFFC.2018.2832600.
- [12] Iman Taghavi et al. “Ultrasound Super-Resolution Imaging with a Hierarchical Kalman Tracker”. In: *Ultrasonics* 122 (May 2022), p. 106695. ISSN: 0041-624X. DOI: 10.1016/j.ultras.2022.106695.
- [13] Shanshan Tang et al. “Kalman Filter-Based Microbubble Tracking for Robust Super-Resolution Ultrasound Microvessel Imaging”. In: *IEEE Transactions on Ultrasonics, Ferroelectrics, and Frequency Control* 67.9 (Sept. 2020), pp. 1738–1751. ISSN: 1525-8955. DOI: 10.1109/TUFFC.2020.2984384.
- [14] Vincent Hingot et al. “Microvascular Flow Dictates the Compromise between Spatial Resolution and Acquisition Time in Ultrasound Localization Microscopy”. In: *Scientific Reports* 9.1 (Feb. 2019), p. 2456. ISSN: 2045-2322. DOI: 10.1038/s41598-018-38349-x.
- [15] Hatim Belgharbi et al. “An Anatomically Realistic Simulation Framework for 3D Ultrasound Localization Microscopy”. In: *IEEE Open Journal of Ultrasonics, Ferroelectrics, and Frequency Control* 3 (2023), pp. 1–13. ISSN: 2694-0884. DOI: 10.1109/OJUFFC.2023.3235766.
- [16] A. Bar-Zion et al. “SUSHI: Sparsity-Based Ultrasound Super-Resolution Hemodynamic Imaging”. In: *IEEE Transactions on Ultrasonics, Ferroelectrics, and Frequency Control* 65.12 (Dec. 2018), pp. 2365–2380. ISSN: 1525-8955. DOI: 10.1109/TUFFC.2018.2873380.
- [17] Chengwu Huang et al. “Short Acquisition Time Super-Resolution Ultrasound Microvessel Imaging via Microbubble Separation”. In: *Scientific Reports* 10.1 (Apr. 2020), p. 6007. ISSN: 2045-2322. DOI: 10.1038/s41598-020-62898-9.
- [18] Alexis Leconte et al. *A Tracking Prior to Localization Workflow for Ultrasound Localization Microscopy*. Aug. 2023. DOI: 10.48550/arXiv.2308.02724. arXiv: 2308.02724 [physics].
- [19] Xin Liu et al. “Deep Learning for Ultrasound Localization Microscopy”. In: *IEEE Transactions on Medical Imaging* 39.10 (Oct. 2020), pp. 3064–3078. ISSN: 1558-254X. DOI: 10.1109/TMI.2020.2986781.
- [20] Ruud J. G. van Sloun et al. “Super-Resolution Ultrasound Localization Microscopy Through Deep Learning”. In: *IEEE Transactions on Medical Imaging* 40.3 (Mar. 2021), pp. 829–839. ISSN: 1558-254X. DOI: 10.1109/TMI.2020.3037790.
- [21] Xi Chen et al. “Deep Learning-Based Microbubble Localization for Ultrasound Localization Microscopy”. In: *IEEE Transactions on Ultrasonics, Ferroelectrics, and Frequency Control* 69.4 (Apr. 2022), pp. 1312–1325. ISSN: 1525-8955. DOI: 10.1109/TUFFC.2022.3152225.
- [22] Léo Milecki et al. “A Deep Learning Framework for Spatiotemporal Ultrasound Localization Microscopy”. In: *IEEE Transactions on Medical Imaging* 40.5 (May 2021), pp. 1428–1437. ISSN: 1558-254X. DOI: 10.1109/TMI.2021.3056951.
- [23] YiRang Shin et al. *Context-Aware Deep Learning Enables High-Efficacy Localization of High Concentration Microbubbles for Super-Resolution Ultrasound Localization Microscopy*. Apr. 2023. DOI: 10.1101/2023.04.21.536599.
- [24] Xi Chen et al. “Localization Free Super-Resolution Microbubble Velocimetry Using a Long Short-Term Memory Neural Network”. In: *IEEE Transactions on Medical Imaging* (2023), pp. 1–1. ISSN: 1558-254X. DOI: 10.1109/TMI.2023.3251197.
- [25] Christopher Choy, JunYoung Gwak, and Silvio Savarese. “4D Spatio-Temporal ConvNets: Minkowski Convolutional Neural Networks”. In: *2019 IEEE/CVF Conference on Computer Vision and Pattern Recognition (CVPR)*. Long Beach, CA, USA: IEEE, June 2019, pp. 3070–3079. ISBN: 978-1-72813-293-8. DOI: 10.1109/CVPR.2019.00319.
- [26] JunYoung Gwak, Christopher Choy, and Silvio Savarese. “Generative Sparse Detection Networks for 3D Single-Shot Object Detection”. In: *Computer Vision – ECCV 2020*. Ed. by Andrea Vedaldi et al. Vol. 12349. Cham: Springer International Publishing, 2020, pp. 297–313. ISBN: 978-3-030-58547-1 978-3-030-58548-8. DOI: 10.1007/978-3-030-58548-8_18.
- [27] Chen-Yu Lee et al. “Deeply-Supervised Nets”. In: *Proceedings of the Eighteenth International Conference on Artificial Intelligence and Statistics*. PMLR, Feb. 2015, pp. 562–570.
- [28] Damien Garcia. “SIMUS: An Open-Source Simulator for Medical Ultrasound Imaging. Part I: Theory & Examples”. In: *Computer Methods and Programs in Biomedicine* 218 (May 2022), p. 106726. ISSN: 0169-2607. DOI: 10.1016/j.cmpb.2022.106726.
- [29] Diederik P. Kingma and Jimmy Ba. *Adam: A Method for Stochastic Optimization*. Jan. 2017. DOI: 10.48550/arXiv.1412.6980. arXiv: 1412.6980 [cs].
- [30] H. W. Kuhn. “The Hungarian Method for the Assignment Problem”. In: *Naval Research Logistics Quarterly* 2.1-2 (1955), pp. 83–97. ISSN: 1931-9193. DOI: 10.1002/nav.3800020109.
- [31] Enrique S. Marquez, Jonathon S. Hare, and Mahesan Niranjan. “Deep Cascade Learning”. In: *IEEE Transactions on Neural Networks and Learning Systems* 29.11

- (Nov. 2018), pp. 5475–5485. ISSN: 2162-237X, 2162-2388. DOI: 10.1109/TNNLS.2018.2805098.
- [32] Artur Speiser et al. “Deep Learning Enables Fast and Dense Single-Molecule Localization with High Accuracy”. In: *Nature Methods* 18.9 (Sept. 2021), pp. 1082–1090. ISSN: 1548-7105. DOI: 10.1038/s41592-021-01236-x.
- [33] Chiheb Trabelsi et al. “Deep Complex Networks”. In: *International Conference on Learning Representations*. Feb. 2018.
- [34] Jingfeng Lu et al. “Complex Convolutional Neural Networks for Ultrafast Ultrasound Imaging Reconstruction From In-Phase/Quadrature Signal”. In: *IEEE Transactions on Ultrasonics, Ferroelectrics, and Frequency Control* 69.2 (Feb. 2022), pp. 592–603. ISSN: 0885-3010, 1525-8955. DOI: 10.1109/TUFFC.2021.3127916.
- [35] Paul Xing et al. “Phase Aberration Correction for in Vivo Ultrasound Localization Microscopy Using a Spatiotemporal Complex-Valued Neural Network”. In: *IEEE Transactions on Medical Imaging* (2023), pp. 1–1. ISSN: 1558-254X. DOI: 10.1109/TMI.2023.3316995.